Electronic Supplementary Material (ESI) for Chemical Communications.

Electronic Supplementary Information

Tandem X-ray absorption spectroscopy and scattering for in situ time-resolved monitoring of gold nanoparticle mechanosynthesis

Paulo F. M. de Oliveira,[*a,b] *Adam A.L. Michalchuk,*[b†] *Ana Guilherme Buzanich,*[b†] *Ralf Bienert,*[b] *Roberto M. Torresi,*[a] *Pedro H. C. Camargo*[a,c] *and Franziska Emmerling**[b]

1 Experimental details

1.1 Chemicals

$HAuCl_4.3H_2O$ (99.9 %, Sigma-Aldrich) was used as gold salt precursor and polyvinylpyrrolidone (PVP; $\overline{Mw}$ 10,000 g.mol^{-1}, Sigma-Aldrich) as stabilizing agent. Three reducing agents were studied: L-ascorbic acid (99%, Sigma-Aldrich), hydroquinone (99 %, Acros Organics) and sodium borohydride ($NaBH_4$, 98 %, Fischer Chemical).

1.2 Ball milling synthesis of Au NPs

Au NPs were synthesized *via* the bottom-up chemical reduction methodology in a ball-milling device. The milling experiments were conducted in a vertical vibratory ball mill (Pulverisette 23, Fritsch) at 50 Hz using custom-made PMMA jars (4.3 cm^3) and one single zirconia milling ball (Ø = 5 mm; 0.41 g). For the synthesis of gold particles, $HAuCl_4.3H_2O$ was used as a gold source. This precursor is mostly dissolved by the atmospheric moisture during manipulation before milling, thereby greatly reducing its crystallinity. To ensure the added amount, the metal precursor was weighted directly in the milling jar. The stabilizing agent (PVP) and gold salt were co-milled prior to the addition of reductant. This pre-milling step ensured the complete dispersion of gold within the polymer matrix. The reducing agent was subsequently added, and the ball milling mechanosynthesis reaction was started. The mechanosynthesis reaction was monitored in real time and *in situ* using tandem synchrotron powder X-ray diffraction (PXRD) and X-ray Absorption Near Edge Structure spectroscopy (XANES) (details in Section 1.3).

Table S1 displays the amount of each component for the different experiments. The values were based on preliminary studies and on the global balanced redox reactions (Eq. 1-3).[1] They were chosen to ensure a reasonable reaction time for time-resolved *in situ* monitoring in the milling conditions we employed. Note the overall amount of powder remained approximately the same for all runs.

Table S1. Composition of mixtures used for mechanochemical synthesis and real-time in situ monitoring of gold nanoparticles.

Reductant R_A	**Reductant (mg)**	**$HAuCl_4.3H_2O$ (mg)**	**PVP (mg)**	**Molar ratio $[AuCl_4]^-$: R_A**	**Theoretical Molar ratio* $[AuCl_4]^-$: R_A**
Hydroquinone	15	36.1	80	2:3	2:3
Ascorbic Acid	48	36.1	50	2:6	2:3
$NaBH_4$	5	41.6	85	2:2.5	2:0.75

* Values based on the global balanced redox equations 1-3

$$2\,AuCl_4^- + 3\,C_6H_8O_6 \rightarrow 2\,Au^0 + 3\,C_6H_6O_6 + 6\,HCl + 2\,Cl^-$$ Eq. (1)

$$2\,AuCl_4^- + 3\,C_6H_4(OH)_2 \rightarrow 2\,Au^0 + 3\,C_6H_4O_2 + 6\,HCl + 2\,Cl^-$$ Eq. (2)

$$8\,AuCl_4^- + 3\,BH_4^- + 9\,H_2O \rightarrow 8\,Au^0 + 3\,B(OH)_3 + 21\,HCl + 11\,Cl^-$$ Eq. (3)

1.3 Time-resolved in situ monitoring (TRIS)

Simultaneous time-resolved *in situ* (TRIS) PXRD and XANES were performed at the *μ*Spot beamline of the Berliner Elektronenspeicherring-Gesellschaft für Synchrotronstrahlung - BESSY II, Berlin-Germany.[2,3] Scheme S1 outlines the *μ*Spot beamline and the experimental setup. For more details, see Ref [4].

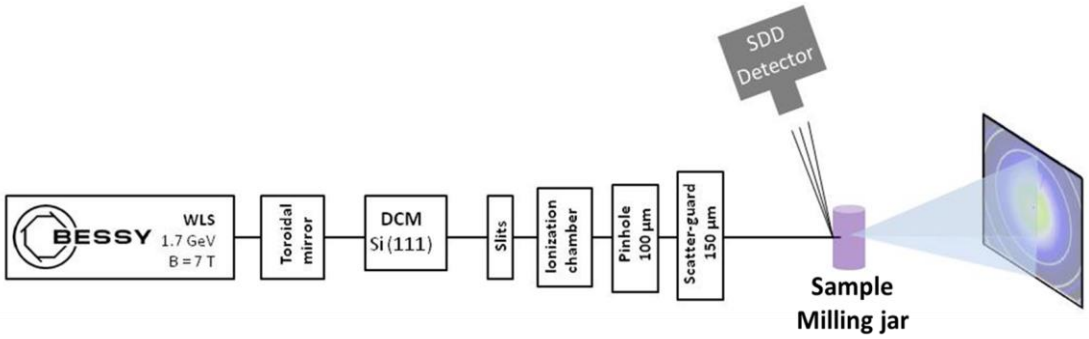

Scheme S1 - Layout of simultaneous XANES experiments in fluorescence mode (SSD, XRF detector) and PXRD at the *μSpot*, BESSY-II.

By convention, PXRD measurements are performed far from the absorption edge of the scattering material. Moreover, to ensure well-defined scattering angles, angle-dispersive PXRD measurements are performed using a monochromatic incident beam. In contrast, XANES is a photon in-photon out spectroscopy and hence requires variation in the energy of the incident beam. These competing requirements imposed some limitations on the tandem combination of TRIS-XAS and TRIS-PXRD. As high-resolution PXRD data were not required, we opted to optimise the TRIS-XANES measurements in this case. Correspondingly data were collected by scanning the incident energy across the X-ray absorption region of the probing element, from 11,897 to 11,938 eV. Collecting PXRD in this way leads to time evolving shift of scattering to lower angles, and hence overall broadening of our integrated Bragg reflections, **Figure S1**. Broadening in this

regard is minimal and it does not affect the overall applicability of our tandem approach for the present application. However, it is important to note that this artificial broadening does not allow for accurate PXRD profile analysis. Intrinsic to time resolved PXRD analysis of ball milling set-ups, additional broadening occurs from multi-site scattering. The incident beam crosses a (minimal) chord distance through the cylindrical milling vessel. Correspondingly, there are at least two sites of scattering (each milling jar wall).[5] This results in additional, artificial peak broadening of the Bragg reflections in the 2D detector image. The exact broadening which results in this case is a function of the distribution of powder within the milling jar and is hence time dependent. Owing to both of these artificial effects, the resulting PXRD data are not amenable to accurate PXRD profile analysis.

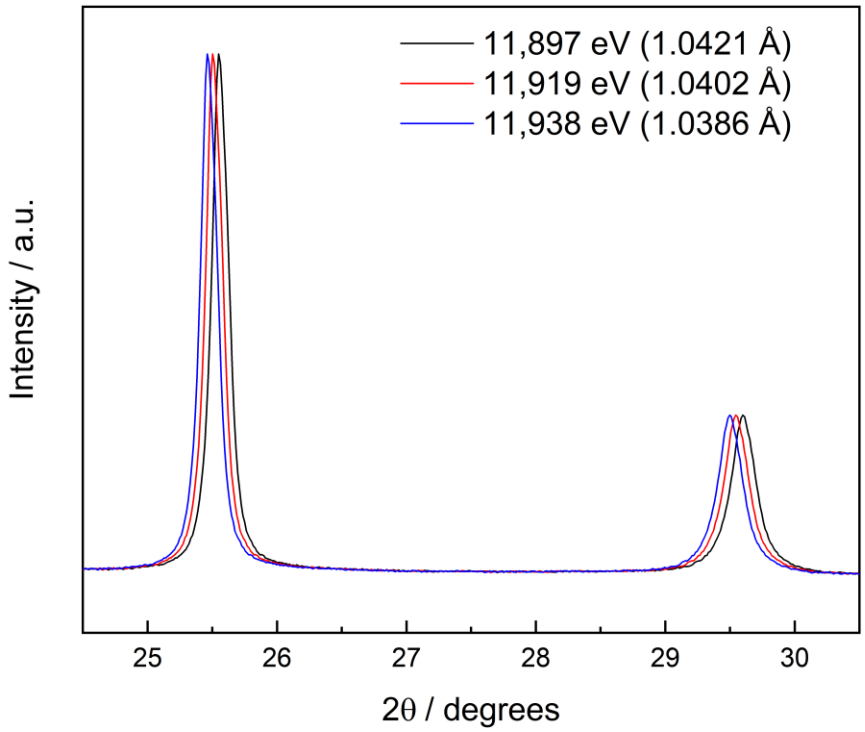

Figure S1. Simulated PXRD at different energies: 11,897 eV (begin of XANES scanning), 11,919 eV (Au-L_{III} edge) and 11,938 eV (end of XANES range).

Collection of X-ray scattering at the absorption edge of the sample is complicated by the high degree of absorption. Organic materials are well known to absorb strongly at these range of photon energies, and hence also absorb a considerable amount of the

incident flux (*ca.* 28 % in our case, only from the PMMA jar). This greatly limits the detection of diffracting species during ball milling, and hence requires long collection times. By keeping the concentration of the organic components as low as possible and the concentration of gold at a reasonable limit, we could acquire successfully both absorption and scattering data from our experiments. To illustrated, **Figure S2** displays the simulation of the transmission of the incident X-rays as function of energy for the three main components of our system: PMMA jar (simulated for wall thickness *ca* 1.5 mm), PVP (simulated with 100 µm thick) and gold salt (simulated with 10 µm thick). It is noticed the abrupt reduction in the transmission around the absorption energy of gold when at Au-L_{III} edge. For applications to other chemical systems or milling set-ups, similar analysis of the beam behaviour (e.g. absorption) is required to assess the feasibility of TRIS-XANES / TRIX-XRD for mechanochemical investigation.

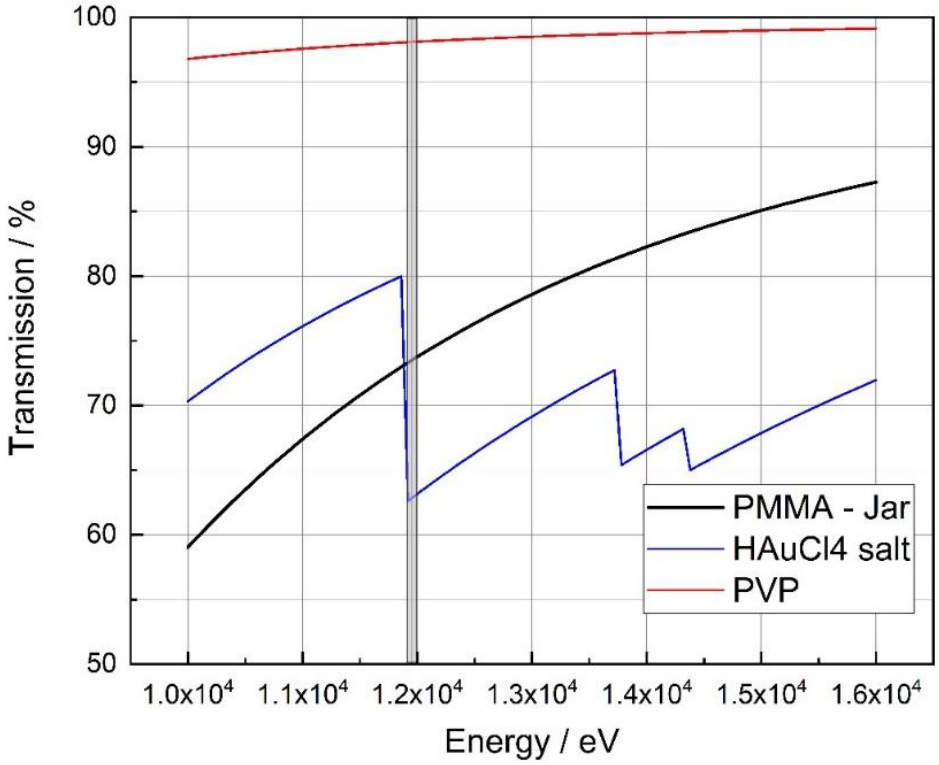

Figure S2. Simulation of the X-ray transmission as function of energy for three main components of the studied systems: PMMA jar, PVP ang gold salt. Note, these simulations stand as illustration only and do not reflect the real thickness of PVP or gold salt in the beam during measurements, which are unknown. The gray window represents the energy scan range used in the measurements. Data simulated in http://henke.lbl.gov/optical_constants/filter2.html according to Ref[6].

1.3.1 X-ray absorption near edge structure spectroscopy (XANES)

The beam was monochromatized using a double-crystal monochromator (DCM) Si (111) installed at the beamline, with a resolution of approximately 2.5 x 10^{-4}, corresponding to 2.8 eV for Au L_3-edge (11,919 eV) at the full width at half maximum (FWHM). The slits were adjusted to provide a 0.7 x 0.7 mm beam size. This was in turn reduced by a pinhole of 150 µm spot size. The scans were performed by tuning the excitation energy between 11,897 eV and 11,938 eV. Energy was varied with 1 eV energy step size and 8 seconds per point for a total of 7.5 minutes per spectrum. The detection was performed in fluorescence. The fluorescence of the Au-Lα line (9.72 keV) was detected with a silicon drift detector (SDD) (AXA, KETEK, Munich, Germany) with a 100 mm^2 active area at a working distance of 50 mm to the sample at 30° with respect to the incident beam.

XANES data were processed using ATHENA, within the IFEFFIT package (v. 1.2.11).[7] The AutoBK background subtraction procedure was used with the Rbkg parameter set to 1.0 Å. Following standard procedures, all spectra were normalized to the pre- and post-edge region. Determination of the edge position was carried out with a gold metal foil. In addition, the Au^{III} standard was measured ($HAuCl_4.3H_2O$). Each XANES spectrum presented in the paper is a result of the sum of two consecutive acquisitions, *i.e.* 2 x 7.5 min (15 min time resolution) and from two repetitions. This means four spectra were used to maximise the signal to noise ratio. Ex situ analysis reveals a slight colour change in the reactions conducted with HQ within the first 5-10 mins of milling. This suggests that the onset of Au reduction in this reaction occurs more quickly than the 15 min time resolution currently possible by TRIS-XAS. Follow up developments in TRS-XAS are evidently required to enhance the time resolution, and will be the study of follow-up investigations. Self-absorption effects were not accounted for in the TRIS-XANES data treatment. As these effects are subtle, they are not expected to have any marked influence on the TRIS-XANES data, as collected here. The same experiments were performed ex-situ and one standard acquisition (ex-situ, also in fluorescence mode) was made by positioning the powder sample between two Kapton® tapes.

1.3.2 Synchrotron powder X-ray diffraction (PXRD)

Scattering data were recorded using an Eiger 9M 2D detector (7.5 min / image, matching with the XANES time scan). The images were integrated using the azimuthal integration as implemented in DPDAK[8] and treated using Powder3D[9] for background subtraction. Time resolved data were visualised using a home-built python code.

The scattering data was recorded simultaneously during energy scanning for XANES spectroscopy. This means that a non-monochromatic beam has been used over the accumulation of each PXRD pattern. As previously mentioned, this results in broadening of the diffraction peaks. **Figure S1** shows a simulated diffraction pattern of gold at different energies – 11,897 eV and 11,938 eV, that corresponds to the scanning range for XANES records. The very slightly broadening does not affect the trend and the information got from the PXRD patterns.

1.4 Complementary characterizations

1.4.1 Transmission Electron Microscopy – TEM

Samples for Transmission Electron Microscopy (TEM) were dispersed in isopropanol, deposited in Carbon-Formvar coated copper grids and dried in air. TEM images were obtained using a Talos F200S microscope (Thermo Scientific) operating at 200 kV.

Figure S3 displays the TEM images of the final samples. In the experimental conditions used, it is possible to see that only the reaction performed using $NaBH_4$ as reducing agent leads to the formation of nanosized gold particles. Hydroquinone and ascorbic acid yield microparticles when used as reducing agents.

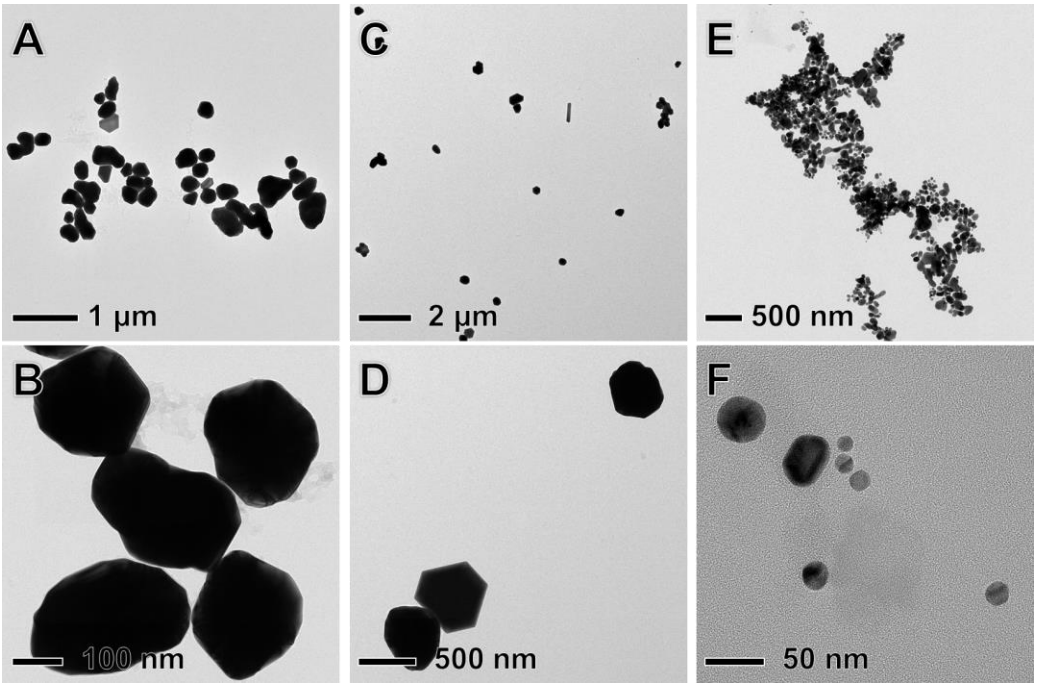

Figure S3. TEM images of gold particles produced during real-time *in situ* monitored ball milling reactions using different reducing agents: hydroquinone (A-B), ascorbic acid (C-D) and $NaBH_4$ (E-F).

1.4.2 Powder X-ray diffraction (PXRD)

Ex-situ PXRD pattern was collected using a Bruker D8 Advance (Bruker AXS GmbH, Germany) in Bragg-Brentano geometry. The samples were measured over a range of 5-80° 2θ (step width 0.02° 2θ, count time 1 s/step).

2 TRIS-PXRD

2.1 2D plots of TRIS-PXRD

Figure S4 displays the TRIS-PXRD data for Au particle formation under milling.

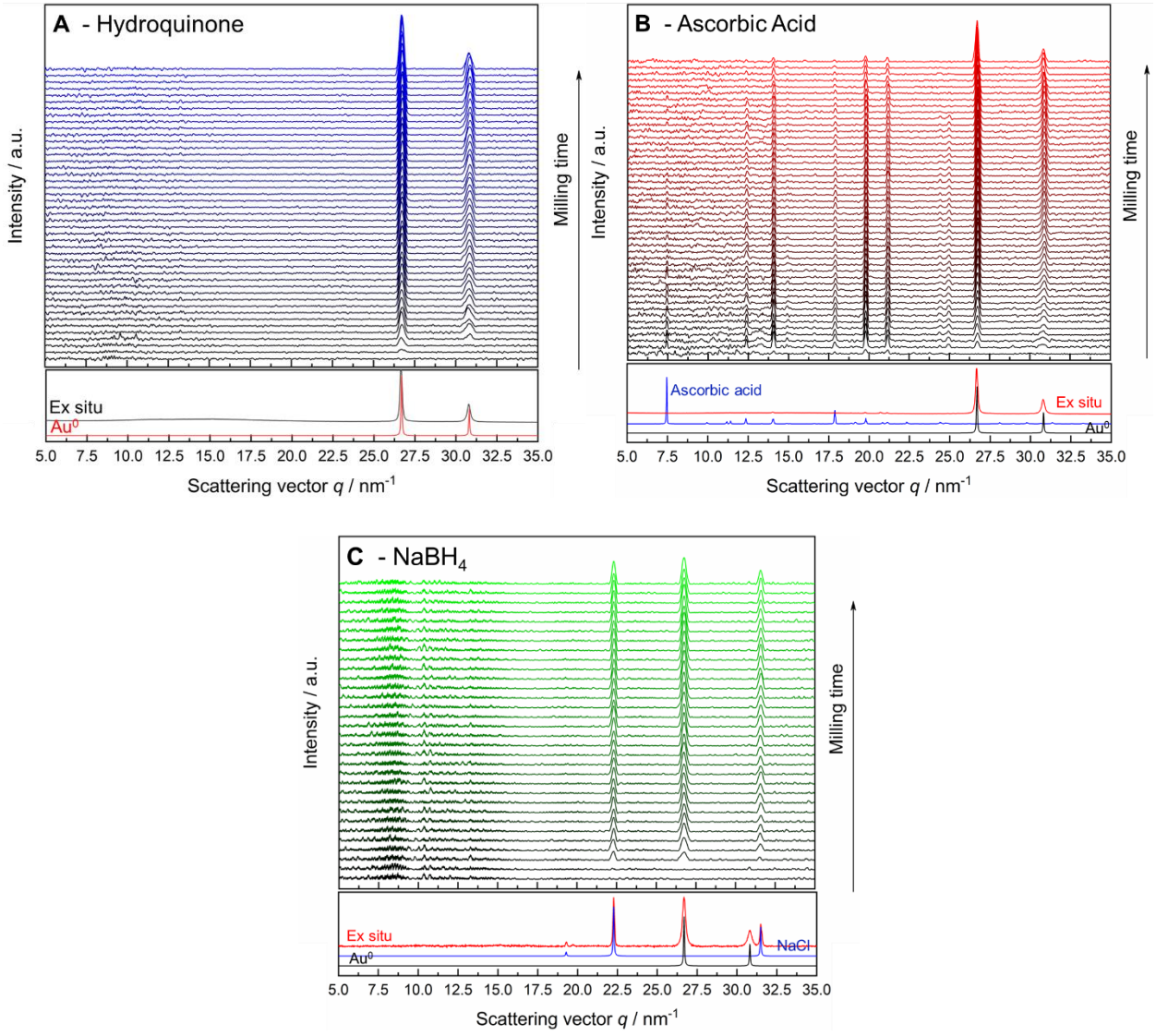

Figure S4. TRIS-PXRD patterns for Au particle formation under milling using different reducing agents: (A) hydroquinone, (B) ascorbic acid, (C) $NaBH_4$. The final ex situ data is also included along with simulated fcc Au phase and the PXRD patterns of ascorbic acid (B) and NaCl (C).

2.2 Integrated peak intensities from TRIS-PXRD

Integration of the major Bragg reflection for Au^0 offers further insight into the dynamics of the bottom-up Au NP mechanochemical synthesis, **Figure S5**. For all three reducing agents, growth starts rapidly, followed by gradual decrease of the reaction rate. The reaction does not go to completion when HQ (A, blue) is used as a reducing agent, as indicated by the continued growth of the Au^0 Bragg reflection. The bottom up synthesis driven by AA (B, red) and $NaBH_4$ (C, green) both reach plateaus, although no clear indication as to whether complete conversion has been achieved. Whereas the onset of reaction in both the HQ and AA-driven mechanosyntheses begin within the first 15 mins, a notable induction period is observed in the case of $NaBH_4$.

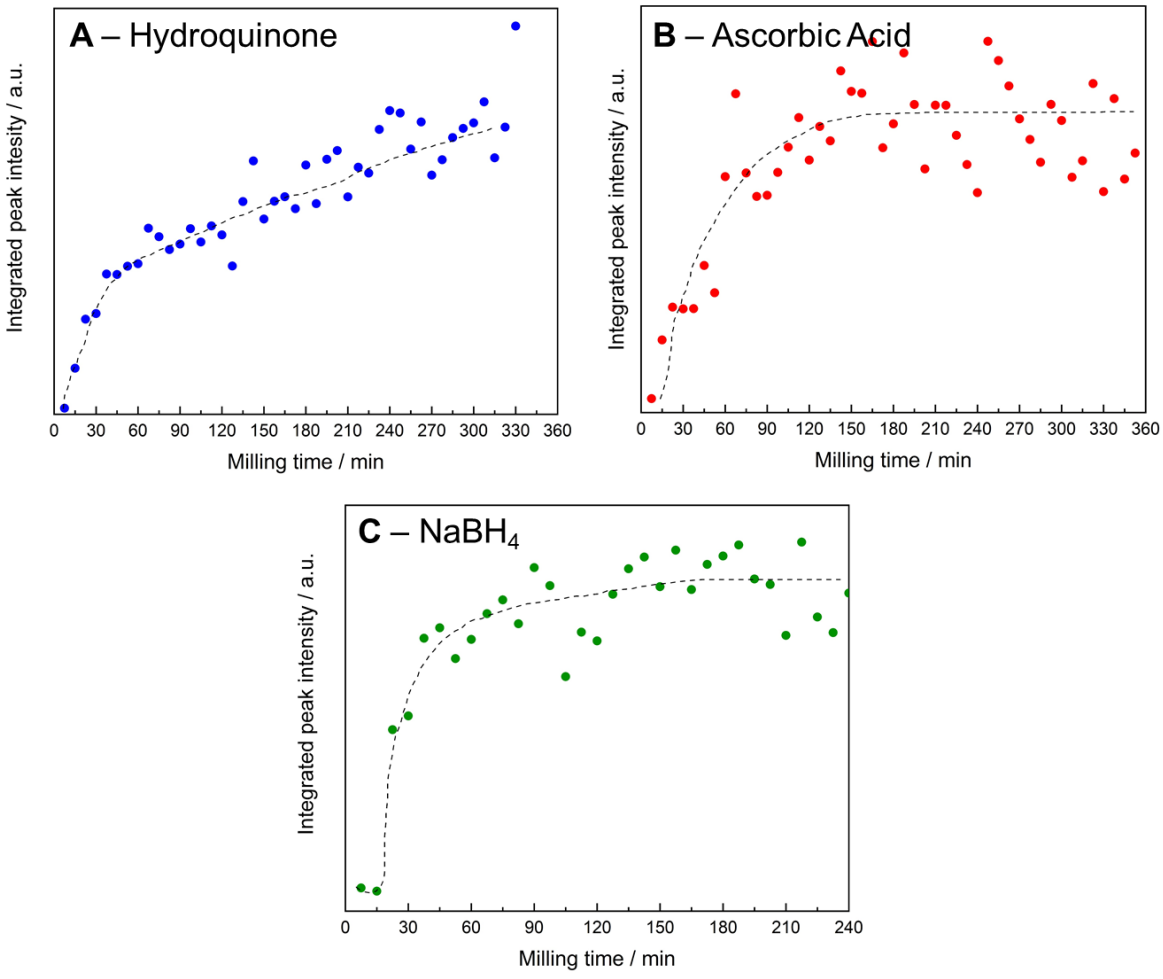

Figure S5. Integrated peak intensities (Au^0, q = 26.7 nm^{-1}) as function of time. The dot lines are merely trends and not a data fit. A – hydroquinone (blue), B – ascorbic acid (red) and C – $NaBH_4$ (green).

2.3 Crystallite size estimation

We have estimated the Scherrer crystallite sizes from the in situ data which are shown in **Figure S6** . The crystallite sizes values of the final product were also obtained from the acquisition in a lab diffractometer in Bragg-Brentano geometry (details in ESI 1.4.2). As we can see below, there is indeed an evolution of the crystallite size as the reaction progresses. However, comparing the final sizes estimated for in situ runs with the values of the ex situ data from the same final product, we see that the ex situ data gives bigger crystallite sizes. Owing the above-mentioned reasons for artificial peak broadening (Section 1.3 and **Figure S1**), in our case the in situ data is therefore not suitable for consistent crystallite sizes estimation in our experimental conditions.

In comparison to TEM images (**Figure S3**), the estimated crystalline sizes from in situ data do not correspond to the size of the particles seen in the TEM images. This is expected once Scherrer equation gives information regarding crystallite sizes, whereas TEM images give particle sizes. Moreover, the larger sizes identified by TEM, as compared with Scherrer analysis, suggest some degree of polycrystallinity in the samples. AA- and HQ-produced particles are in the order of microns and $NaBH_4$ yields NPs of 25 – 50 nm.

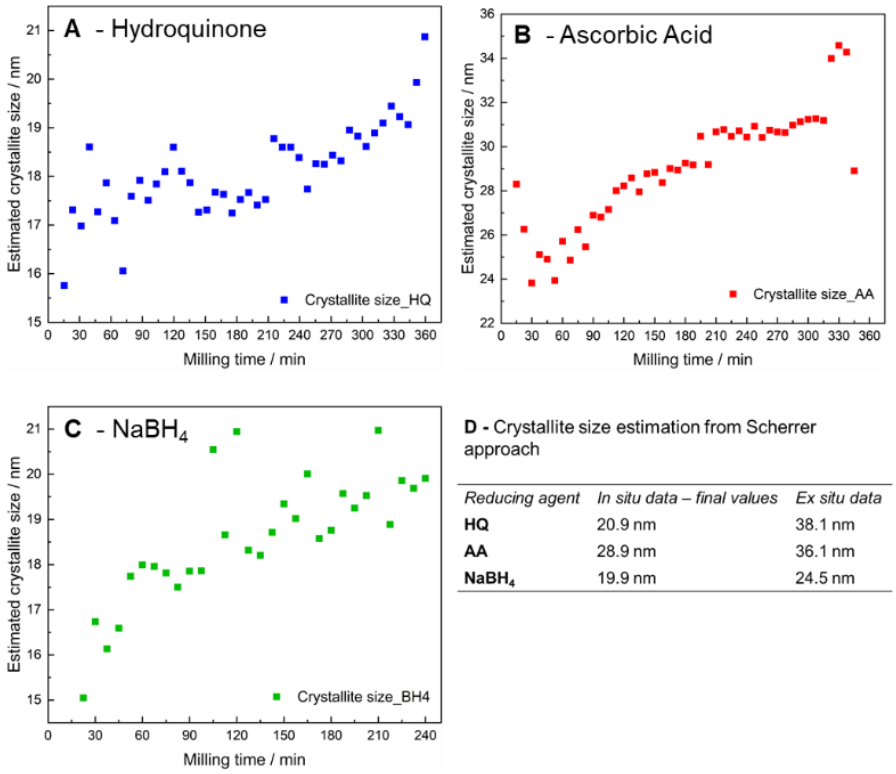

D - Crystallite size estimation from Scherrer approach

Reducing agent	*In situ data – final values*	*Ex situ data*
HQ	20.9 nm	38.1 nm
AA	28.9 nm	36.1 nm
$NaBH_4$	19.9 nm	24.5 nm

Figure S6. Crystallite size estimation according to Scherrer equation. Au particles synthesized using (A) hydroquinone (HQ), (B) ascorbic acid (AA) and (C) $NaBH_4$ as reducing agent. (D) Final crystallite sizes values from in situ and ex situ data.

3 Ex-situ data

3.1 XANES

The XANES of the final samples were again measured in fluorescence mode. The samples were placed in PMMA samples holder and sealed using Kapton® tape. **Figure S7** shows the XANES data for the final samples along with the standard Au^{III} ($HAuCl_4.3H_2O$) (gray) and Au^0 (metal foil) (black). It is possible to see that for hydroquinone (blue) and $NaBH_4$ (green) the final samples are composed by mix of Au^0 and remaining oxidized species. In the case of ascorbic acid (red), indeed, by the end of 360 min of milling, this reductant was able to reduce almost all gold precursor of the medium and the final spectra is very close to the Au^0 standard foil. These results fully support the in-situ data.

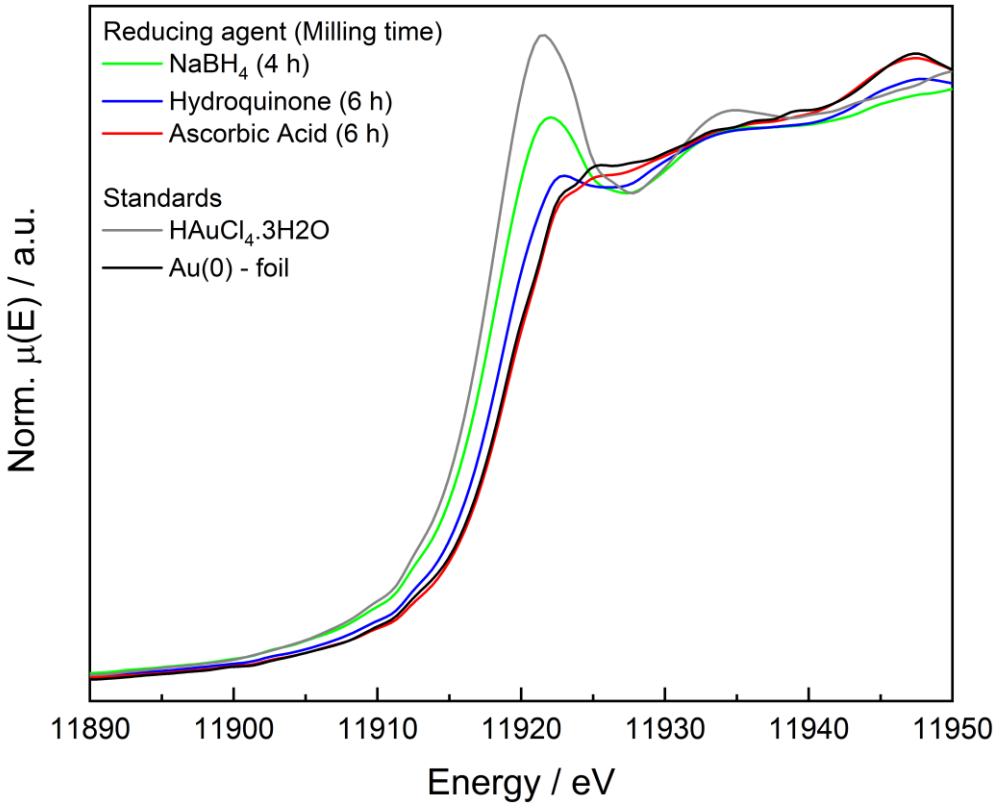

Figure S7. Ex-situ XANES at Au-LIII edge after the milling period (4 h – NaBH4 and 6 h when hydroquinone and ascorbic acid were used) for the reactions with different reducing agents along with Au^{III} and Au^0 standards.

3.2 PXRD

The comparison of PXRD patterns of raw in situ data (no background subtraction), ex-situ and simulated patterns shows that crystalline gold was formed regardless of the reducing agent (**Figures S8-10**). Furthermore, it is also possible to see that some ascorbic acid remains after complete reduction of Au^{III} (**Figure S9**). This is expected as it was added in excess. Finally, it is confirmed that the chemical reduction of $AuCl_4^-$ by $NaBH_4$ generates NaCl as side product (**Figure S10**).

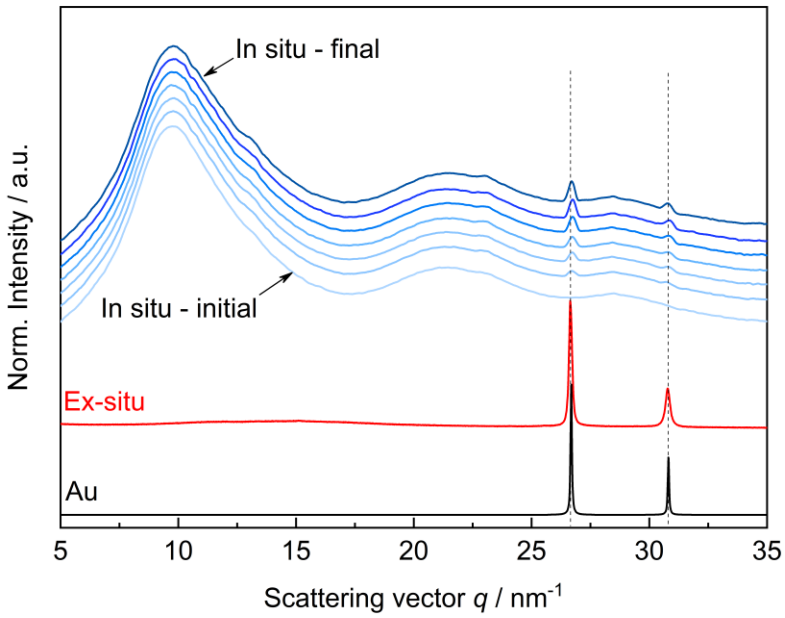

Figure S8. Comparison of XRD patterns of the Au particle synthesis using hydroquinone (HQ) as reducing agent. The in-situ data has no background correction. XRD Au pattern is simulated.

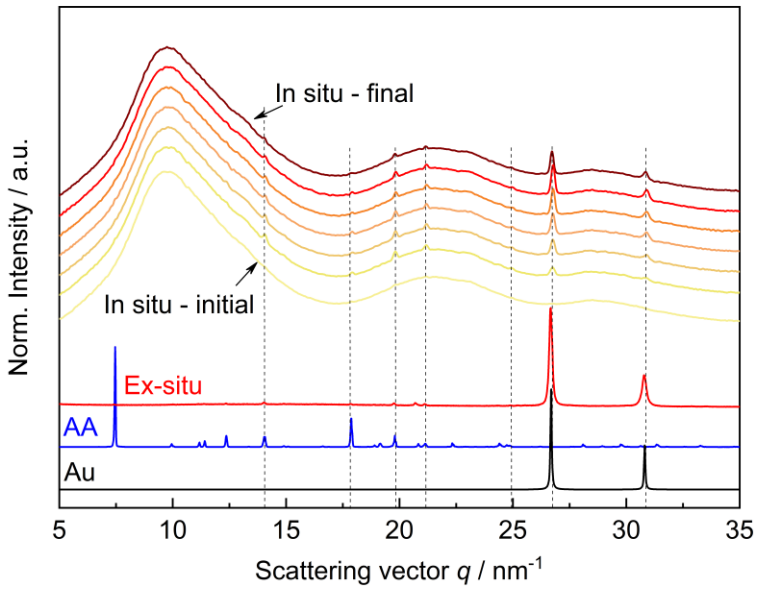

Figure S9. Comparison of XRD patterns of the Au particle synthesis using ascorbic acid (AA) as reducing agent. The in-situ data has no background correction. XRD Au pattern is simulated.

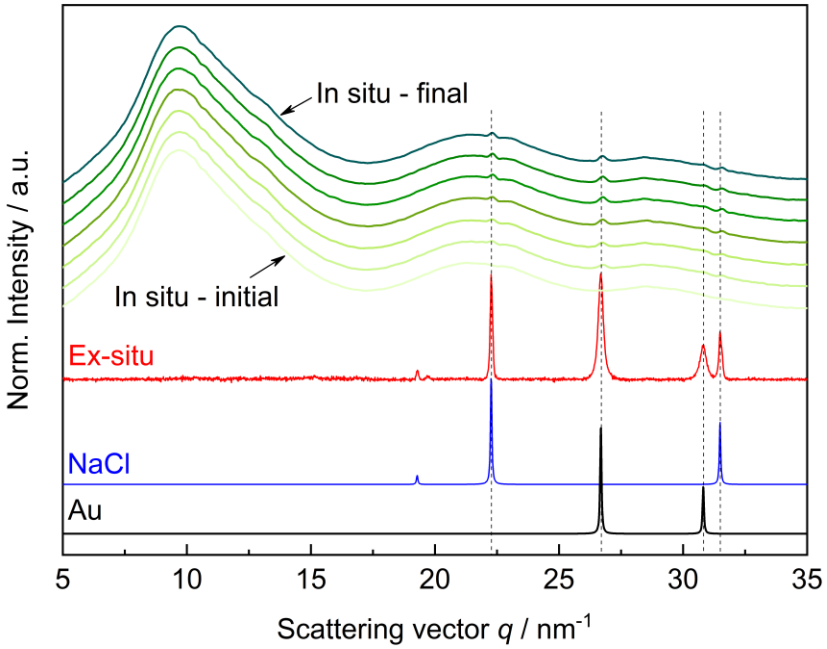

Figure S10. Comparison of XRD patterns of the Au particle synthesis using $NaBH_4$ as reducing agent. The in-situ data has no background correction. XRD of Au and NaCl patterns are simulated.

4 References

[1] T. S. Rodrigues, M. Zhao, T. Yang, K. D. Gilroy, A. G. M. da Silva, P. H. C. Camargo, Y. Xia, *Chem. – A Eur. J.* **2018**, *24*, 16944–16963.

[2] O. Paris, C. Li, S. Siegel, G. Weseloh, F. Emmerling, H. Riesemeier, A. Erko, P. Fratzl, *J. Appl. Crystallogr.* **2006**, *40*, s466–s470.

[3] A. Kabelitz, A. Guilherme, M. Joester, U. Reinholz, M. Radtke, R. Bienert, K. Schulz, R. Schmack, R. Kraehnert, F. Emmerling, *CrystEngComm* **2015**, *17*, 8463–8470.

[4] L. Batzdorf, F. Fischer, M. Wilke, K.-J. Wenzel, F. Emmerling, *Angew. Chemie Int. Ed.* **2015**, *54*, 1799–1802.

[5] T. Friščić, I. Halasz, P. J. Beldon, A. M. Belenguer, F. Adams, S. a J. Kimber, V. Honkimäki, R. E. Dinnebier, *Nat. Chem.* **2013**, *5*, 66–73.

[6] B. L. Henke, E. M. Gullikson, J. C. Davis, *At. Data Nucl. Data Tables* **1993**, *54*, 181–342.

[7] B. Ravel, M. Newville, *J. Synchrotron Radiat.* **2005**, *12*, 537–541.

[8] G. Benecke, W. Wagermaier, C. Li, M. Schwartzkopf, G. Flucke, R. Hoerth, I. Zizak, M. Burghammer, E. Metwalli, P. Müller-Buschbaum, et al., *J. Appl. Crystallogr.* **2014**, *47*, 1797–1803.

[9] B. Hinrichsen, R. E. Dinnebier, P. Rajiv, M. Jansen, **2008**.